Anisotropic silk nanofiber layers as regulators of angiogenesis for optimized bone regeneration

Zhihai Fan [a],[1], Hongxiang Liu [a],[1], Shilei Shi [a], Zhaozhao Ding [b],[**], Zhen Zhang [c], Qiang Lu [b],[*], David L. Kaplan [d]

[a] Department of Orthopedics, The Second Affiliated Hospital of Soochow University, Soochow University, Suzhou, 215000, PR China
[b] National Engineering Laboratory for Modern Silk & Collaborative Innovation Center of Suzhou Nano Science and Technology, Soochow University, Suzhou, 215123, PR China
[c] Department of Dermatology, Shanghai Ninth People's Hospital, Shanghai Jiaotong University School of Medicine, Shanghai, 200011, PR China
[d] Department of Biomedical Engineering, Tufts University, Medford, MA, 02155, United States

ARTICLE INFO

ABSTRACT

Osteogenesis-angiogenesis coupling processes play a crucial role in bone regeneration. Here, electric field induced aligned nanofiber layers with tunable thickness were coated on the surface of pore walls inside the deferoxamine (DFO)-laden silk fibroin (SF) and hydroxyapatite (HA) composite scaffolds to regulate the release of DFO to control vascularization dynamically. Longer electric field treatments resulted in gradually thickening layers to reduce the release rate of DFO where the released amount of DFO decreased gradually from 84% to 63% after 28 days. Besides the osteogenic capacity of HA, the changeable release of DFO brought different angiogenic behaviors in bone regeneration process, which provided a desirable niche with osteogenic and angiogenic cues. Anisotropic cues were introduced to facilitate cell migration inside the scaffolds. Changeable cytokine secretion from endothelial cells cultured in the different scaffolds revealed the regulation of cell responses related to vascularization *in vitro*. Peak expression of angiogenic factors appeared at days 7, 21 and 35 for endothelial cells cultured in the scaffolds with different silk nanofier layers, suggesting the dynamical regulation of angiogenesis. Although all of the scaffolds had the same silk and HA composition, *in vitro* cell studies indicated different osteogenic capacities for the scaffolds, suggesting that the regulation of DFO release also influenced osteogenesis outcomes *in vitro*. *In vivo*, the best bone regeneration occurred in defects treated with the composite scaffolds that exhibited the best osteogenic capacity *in vitro*. Using a rat bone defect model, healing was achieved within 12 weeks, superior to those treated with previous SF-HA composite matrices. Controlling angiogenic properties of bone biomaterials dynamically is an effective strategy to improve bone regeneration capacity.

1. Introduction

Bone regeneration is a complex and well-orchestrated process that involves a series of cell responses and molecular signaling pathways [1–3]. Angiogenesis and osteogenesis are major determinants of successful bone repair and these processes have been regulated by introducing multiple physical/chemical cues to bone biomaterials to study the impact *in vivo* [4–7]. Although faster and better bone regeneration has been achieved based on these bioactive biomaterial matrices, challenges remain to tune angiogenesis and osteogenesis outcomes in a dynamic way to simulate the different stages of the natural bone regeneration process [8].

Silk fibroin (SF) biomaterials are promising bone regenerative matrices due to the biocompatibility, excellent and tunable mechanical properties, and ease of materials fabrication [9–12]. SF-based scaffolds, films and hydrogels have been developed to repair various bone defects [9,13–15]. The cytocompatibility and bioactivity of these matrices were further improved by changing nano-micro structures, anisotropic topography, degradation behavior and mechanical performance [16–19]. Various polymers, mineral nanomaterials, and biomacromolecules were also

introduced into silk-based bone matrices, endowing them with angiogenesis and osteogenesis inducing and control features [5,20,21]. However, a gap maintains for SF matrices to further improve the angiogenic and osteogenic capacity in a dynamic fashion for bone regeneration.

Recently, SF nanofibers (SFNs) were assembled to develop biomimetic matrices [22–24]. Owing to the unique hydrophilic/hydrophobic properties, these SFNs could be loaded with both hydrophilic and hydrophobic cargos, suggesting a promising future as drug carriers [25,26]. SFNs were then used to design various bioactive artificial bones. SFN and hydroxyapatite (HA) were blended to prepare composite scaffolds with osteogenic capacity [27]. Deferoxamine (DFO) was loaded onto the SNFs and further mixed with HA, forming hydrogels with angiogenic and osteogenic capacities [5]. Both *in vitro* and *in vivo* studies revealed that the DFO sustained release features determined angiogenesis, but did not fully control angiogenesis in a dynamic fashion matched with natural bone healing process. Anisotropic silk hydrogels derived from SFN solutions under electric fields directionally aligned the components on the positive electrode [28–30]. This study suggested that nanofiber layers with control of thickness could be prepared by adjusting the experimental time, followed by covering the surface of DFO-laden composite scaffolds, as a route to tune the release behavior of DFO.

Thus, as a proof of concept, DFO-laden SF-HA composite scaffolds were immersed in SFN solutions and treated under electric fields to form aligned layers on the surface of pore walls inside the scaffolds (Scheme 1). The microstructure and thickness of the layers were controlled with treatment time, resulting in different sustained release behaviors. To the best of our knowledge, it is the first time to tune the sustained release behaviors of DFO dynamically in silk-based porous scaffolds used in bone repair. The aligned topography also induced the migration of cells, which further accelerated bone regeneration, as has been shown previously with aligned scaffolds [28]. Both *in vitro* and *in vivo* studies revealed that the best angiogenesis and osteogenesis for bone repair was achieved with suitable DFO sustained release conditions when the pore walls of the scaffolds were covered with aligned silk nanofiber layer treated in electric field for 10 min. Our present results implied that the angiogenic behaviors in bone regeneration process could be regulated to further optimize bone repair, opening a new window to design bone materials with vascularization capacity. Faster and higher quality bone regeneration was regulated by angiogenesis, implying future utility in clinical applications.

2. Material and methods

2.1. Preparation of aqueous silk fibroin (SF) solutions

Aqueous SF solutions were obtained by dissolving degummed silk in lithium bromide solution [31]. Briefly, raw silk was boiled in an aqueous solution of sodium carbonate (0.02 M) at 100 °C for 60 min and washed with distilled water to degum the sericin protein. The degummed silk was dissolved in lithium bromide (9.3 M) at 60 °C for 4 h, and dialyzed against deionized water to remove the salts for more than 72 h. After centrifugation twice at 9000 rpm for 30 min at 4 °C, a fresh aqueous SF solution with a concentration of about 6 wt % was obtained. The SF solution was stored at 4 °C for further use.

### 2.2. Preparation of SF nanofiber (SFN) hydrogel

The SF nanofibers were assembled through the concentration-dilution-thermal incubation process [30]. The SF molecules were self-assembled into metastable particles with the size of 100 nm after being concentrated to above 20% slowly at 60 °C for about 72 h. Then the particles transformed into stable nanofibers when the concentrated solution was diluted to 0.5 wt% and 2 wt% with distilled water and incubated at 60 °C to induce the hydrogel formation.

2.3. Fabrication of SF-coated HA nanoparticles

SF-coated HA nanoparticles were fabricated using SF as a template and surface stabilizer [32]. Fresh SF (6 wt%) was incubated at 60 °C for 24 h to generate homogeneous silk nanoparticles. Then silk nanoparticle solution (20 mL) was mixed with H_3PO_4 solutions (20 mL, 0.06 M), followed by the addition of $Ca(OH)_2$ solution (100 mL, 0.02 M) at 90 mL h^{-1} with vigorous stirring in a water bath at 70 °C. A suitable content of NaOH (0.1 M) was added to adjust the pH of the reaction system to 9–10. The SF-coated HA nanoparticles were collected after centrifugation at 9000 rpm for 20 min.

2.4. Fabrication of DFO-loaded SF-HA composite scaffolds

Porous SF-HA composite scaffolds were fabricated using a modified freeze-drying method [33]. SF solution (6.4 wt%) and SFN hydrogel (2
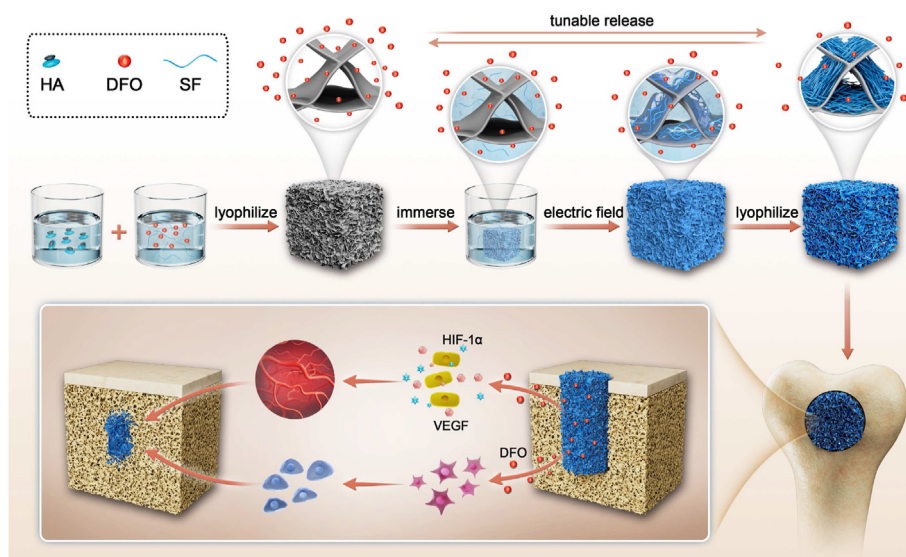
Scheme 1. Formation of DFO-laden SF-HA composite scaffolds with tunable aligned silk nanofiber layers. The release behavior of DFO was controlled through the nanofiber layers to tune angiogenesis, optimizing bone regeneration.

wt%) were mixed at a dry weight ratio of 15:1 to form the composite solution. The SF concentration in the composite solution was adjusted to 1.5 wt% with distilled water. Then HA nanoparticles were added to the composite solution at a dry weight of ratio of 60:40 (SF: HA) under stirring to achieve a uniform mixture. The mixture was frozen in a freezer at −20 °C for 12 h to solidify the solvent and then lyophilized for 72 h. The water-insoluble SF-HA composite scaffolds (SF/HA-R) were obtained after the lyophilization. DFO (120 μM) was also added to the mixture of HA, SF and SFN solution under stirring and then lyophilized for 72 h to prepare DFO-laden composite scaffolds (SF/HA-DFO-R). The SF/HA-DFO-R composite scaffolds were immersed in SFN solution (0.5 wt%) for above 30 min to make sure that all the pores inside the scaffolds were occupied by the SFN solution. Then the SFN solution and the immersed scaffolds were treated under electric field with voltage of 50 V for 5, 10, 15 min to induce the SFN migration, forming SFN hydrogel layers with different thickness on the pore surface inside the scaffolds [29,30]. The treated scaffolds with SFN hydrogel layers were lyophilized for 72 h to obtain the final scaffolds with SFN layers. According to the treating time in electric field, the scaffolds were termed SF-/HA-DFO-A5, SF-/HA-DFO-A10, and SF-/HA-DFO-A15, respectively.

2.5. Fabrication of aligned SFN layers

To evaluate the formation of homogeneous aligned SFN layers inside the scaffolds, three water insoluble films were placed in SFN solution (0.5 wt%) at different positions parallel to the electrodes. Then the SFN solutions were treated with electrical fields with voltage of 50 V for 5, 10, 15 min, respectively. The layers formed on the SF films were investigated to reveal the influence of different positions and treatment times.

2.6. Characterization of the composite scaffolds

The micromorphology of the different scaffolds were observed with a scanning electron microscope (SEM, S-4800, Hitachi, Tokyo, Japan) at 3.0 kV. Before investigation, the samples were sputter-coated with gold (10 mA, 120s) [34]. The thinknesses of different samples were analyzed via Image J. The secondary structure of the different scaffolds was analyzed by Fourier Transform Infrared Spectroscopy (FTIR, Nicolet 5700, Thermo Scientific, FL, America) where 64 scans were run in the wavenumber range 400–4000 cm^{-1}. Raman spectrometry (633 nm diode laser, Renishaw, New Mills, UK) was used to record raman spectra. A 633 nm laser was used with exposure time of 5 s and laser power of 50% with a resolution of 1 cm^{-1}.

2.7. The release of DFO from the scaffolds

The release of DFO in electrical field treatment process was evaluated by measuring the DFO amount in the SFN solution after the electrical field treatment. The SFN solution was combined with ferric chloride to determine the amount of DFO using multiscan spectra at 485 nm (Biotek, USA). Then, All the DFO-laden scaffolds were transferred to a dialysis tube (2000-MWCO) and incubated with phosphate-buffered saline solution (PBS, 10 mL) at 37 °C in an oscillating water bath for 42 days. At the indicated time points, 1 mL of solution in each tube was collected and then refilled with an equal amount of fresh PBS. The collected PBS was combined with ferric chloride to determine the amount of released DFO using multiscan spectra at 485 nm (Biotek, USA).

2.8. Mechanical properties of the scaffolds

Mechanical properties of the different scaffolds were measured with Food Texture Analyzers (TMS-Pro, FTC, USA). Three scaffolds for each group were compressed parallel to and orthogonal to the electric field direction, respectively, to characterize the mechanical anisotropy of scaffolds. The scaffolds (14 mm in diameter and 9 mm in height) were compressed by more than 30% of its original length at the rate of 2 mm/min with a 25 N load cell.

2.9. Degradation behavior of the scaffolds

The *in vitro* degradation of different scaffolds was evaluated using enzyme-promoted degradation. All the scaffolds (30 mg) were soaked in protease XIV solutions with the concentration of 2 U/mL in PBS, and kept at 37 °C in a shaking water bath. At designed time points, the scaffolds were washed with distilled water and dried at 60 °C for above 24 h. Three repeated measurements were obtained for each time point. The degradation rate was calculated through the following formula:

$$\varepsilon(\%)=(m_i-m_r)/ m_i \times 100\%$$

Where ε expressed the degraded rate of the scaffold, m_i represented the initial mass of the scaffold, while m_r was the mass of remaining scaffold after various degradation periods.

2.10. In vitro cytocompatibility of the scaffolds

The *in vitro* cytocompatibility of the composite scaffolds was assessed with human umbilical vein endothelial cells (HUVECs, obtained from the Cell Bank of the Chinese Academy of Sciences, Shanghai, China). All the composite scaffolds with diameter of 10 mm and height of 2 mm were prepared and sterilized with ^{60}Co γ-irradiation at the dose of 25 kGY. The cells were seeded in different scaffolds at a cell density of 1×10^5, and supplied with basal culture medium. HUVECs were cultured in Dulbecco's modified Eagle medium (DMEM, high glucose) supplemented with 10% fetal bovine serum (FBS), 100 U/mL penicillin-streptomycin (all from Invitrogen, Carlsbad, CA) in a cell incubator at 37 °C and under 5% CO_2. After culturing for 1, 3 and 7 d, the scaffolds were washed three times with PBS (pH 7.4) and then fixed with 4% paraformaldehyde solution (Sigma-Aldrich, St. Louis, MO, USA) for 30 min at room temperature. After permeabilization with 0.1% (v/v) Triton X-100 (Sigma, St Louis, USA) for 15 min, the cells were stained for F-actin using tetramethylrhodamine (TRITC)-phalloidin (Thermo Fisher, Waltham, MA, USA) for 1h, and nuclei were stained with 4′,6-diamidino-2-phenylindole (DAPI) for 10 min. All staining treatments were performed in the darkness at room temperature. Finally, fluorescence images of the stained cells were obtained using a confocal laser scanning microscope (CLSM, Olympus FV10 inverted microscope, Nagano, Japan). Cell proliferation was analyzed by DNA content assay at days 1, 3 and 7. All the scaffolds were digested with proteinase K overnight at 56 °C [35]. The DNA content was analyzed by using the PicoGreen DNA assay (Invitrogen, Carlsbad, CA, USA) and measured with a BioTeK Synergy 4 spectrofluorometer (BioTeK, Winooski, VT, USA) at the excitation wavelength of 480 nm and the emission wavelength of 530 nm. A standard curve was obtained to calculate the amount of DNA.

2.11. The migration behavior of HUVECs

To assess cell migration behavior, HUVECs (2×10^6/scaffold) were seeded at the scaffold centers [36]. At specified times, all scaffolds were fixed and stained for observation using CLSM. The distances between the initial edges and migrated cells were measured using Image J software, and the data were presented as a histogram of frequency versus distance (n = 40).

2.12. Tube formation assay

To estimate the angiogenic ability of released DFO, growth factor-reduced Matrigel (100 μL per well, BD Biosciences, Beford, MA, USA) was used to induce tube formation in a 24-well plate [37]. After incubating in 37 °C for 1 h, HUVECs were seeded on the surface of the

Matrigel with cell density of 6×10^4 cell/each well, with the scaffolds placed in the upper compartment of a 0.4 μm Transwell (Corning, USA). Then the cells were incubated at 37 °C to form tube-like structures. After being cultured for 6 and 24 h, the cells were observed with an inverted fluorescence microscope (10× objective, ZEISS camera, Oberkochen, Germany). Based on the previous study [5], the tube length and mesh area were calculated from three random fields using Image J software.

2.13. Assay of angiogenic factors

HUVECs were cultured in the scaffolds with 6-wells plates for 7, 21 and 35 d, and then the scaffolds and the culture solutions were collected in 1.5 mL Eppendorf tubes at the indicated time points. The collected scaffolds were frozen at −80 °C for 12 h, lyophilized for 72 h and stored at −80 °C until proteins were extracted with RIPA lysis buffer. Then proteins were quantified with BCA assay (Thermo Scientific, Waltham, MA, USA). The culture solutions were also stored at −80 °C for further determination of the total released amounts of VEGF (vascular endothelial growth factor) with a Human VEGF Quantikine ELISA kit (R&D Systems, Minneapolis, MN, USA). Total proteins were analyzed to determine the expression of HIF-1α with ELISA (Human/Mouse Total HIF-1α; R&D Systems, Minneapolis, MN, USA).

2.14. Cell osteodifferentiation in vitro

Bone mesenchymal stem cells (BMSCs) were isolated from male Sprague-Dawley (SD) rats (40 g). The use of animals was approved by the animal ethics committee of Soochow University and performed according to the guidelines for care and use of laboratory animals of Soochow University (202103A113, Mar 2021). BMSCs were cultured in Dulbecco's modified Eagle medium (DMEM, low glucose) supplemented with 10% fetal bovine serum (FBS), 100 U/mL penicillin-streptomycin (all from Invitrogen, Carlsbad, CA) in a cell incubator at 37 °C and under 5% CO_2. The seeded BMSCs (5×10^5 cells per well) were cultured in osteogenic differentiation medium (89% low glucose-DMEM, 10% FBS, 1% streptomycin-penicillin, 10 nM dexamethasone, 0.05 mM ascorbic acid-2-phosphate, and 10 mM sodium-β-glycerophosphate) for 3, 7, 14 and 21 days, respectively. According to the method mentioned above [29, 30], the total proteins were extracted from the scaffolds for further tests.

To measure alkaline phosphatase (ALP) activity, cell lysates were tested with an ALP activity assays kit (Biovision, San Francisco, USA) according to the manual. The protein solutions were diluted into 80 μL and mixed with 50 μL p-nitrophenol phosphate substrate (pNPP, 5 mM). After incubated in a 96-well plate at 25 °C for 1 h in the darkness, 20 μL of NaOH solution (2 M) was added to stop the reaction. The production of p-nitrophenol (pNP) was calculated according to the absorbance intensity at 405 nm on a microplate reader. The ALP activity could be normalized based on the total protein content that was determined by BCA assay. To measure the calcium content inside the cell lysates, the proteins were tested with a calcium colorimetric assay kit (Biovision, San Francisco, CA, USA) according to the manufacturer's instructions.

The collected proteins were also analyzed with Western Blot. Each protein sample was treated with SDS electrophoresis and then transferred to a polyvinylidene difluoride membrane (0.45 μm, Millipore, USA). The membranes were blocked with 5% skim milk for 90 min, and incubated overnight at 4 °C with primary antibodies as follows: 1:1000, Anti-RUNX-2 antibody (ab236639, Abcam, Cambridge, MA, USA); 1:1000, Anti-OCN antibody (ab133612, Abcam, Cambridge, MA, USA) after being blocked with 5% skim milk. The β-actin Monoclonal Antibody (1:500, RLM3028, RuiYingBio, China) were also used. The expressions of runt-related transcription factor 2 (Runx-2) and osteocalcin (OCN) from the western blotting images were measured via Image J.

To evaluate osteogenic related gene expression (Runx-2 and OCN), total cellular RNA was extracted with Trizol reagent (Invitrogen, Carlsbad, CA, USA). Then the extracted RNA was purified with a RNeasy Mini Kit (Applied Biosystems, Carlsbad, CA, USA). The RNA concentration was

Table 1
Sequences of primers used in RT-PCR.

Gene	Forward primer sequence (5' to 3')	Reverse primer sequence (5' to 3')
GAPDH	TGGGTGTGAACCACGAGAA	GGCATGGACTGTGGTCATGA
RUNX-2	CAACCACAGAACCACAAGTGC	AAATGACTCGGTTGGTCTCG
Osteocalcin	TATGGCACCACCGTTTAGGG	GTGTGCCGTCCATACTTTCG

determined with Nano Drop 2000 (Thermo Scientific, Waltham, MA). 1 mg of the extracted total RNA was reverse transcribed into complementary DNA (cDNA) by using a High Capacity cDNA Reverse Transcription kit (Applied Biosystems, Carlsbad, CA) with a 2720 thermal cycler (Applied Biosystems, Foster City, CA, USA). A 7500 Real-Time PCR System (Applied Biosystems, Foster City, CA, USA) was used to obtain the real-time PCR results with the Fast SYBR Green kit (Applied Biosystems, Carlsbad, CA, USA). The reaction conditions were as follows: 95 °C (5 min), 40 cycles at 95 °C (10 s) and 60 °C (1 min). The housekeeping gene glyceraldehyde-3-phosphate dehydrogenase (GAPDH) was set as the internal control, and the primer sequences were listed in Table 1. The target gene expression level was calculated with reference to the respective control group based on the 2-ΔΔCt formula.

### 2.15. The construction of bone defect model

A rat femur defect model was used to evaluate the osteoinduction of the composite scaffolds *in vivo*. Forty-eight SD rats (8-week-old, male, 250–300 g) were purchased from the Animal Resource Center of Soochow University. The rats were divided into 6 groups at random: Blank, SF/HA-R, SF/HA-DFO-R, SF/HA-DFO-A5, SF/HA-DFO-A10, SF/HA-DFO-A15. All procedures were approved by the animal ethics committee of Soochow University and performed in conformity to the guidelines for care and use of laboratory animals of Soochow University (201908A166, Aug 2019). Each rat was anesthetized with 3% pentobarbital sodium at 0.1 mL/100 g. After being shaved, the surgery was conducted in a perpendicular orientation on the side face of the bilateral distal femur with a 3 mm diameter injury. The femur defect model was filled with different scaffolds with diameter of 3 mm and height of 5 mm. The defects were sutured with 3–0 stylolite and sterilized with povidone iodine. After operation, the rats were raised for 3 months in pathogen free (SPF) laboratory animal room. At 2, 4, 8 and 12 weeks, the rats were sacrificed using 3% pentobarbital sodium to obtain specimens.

2.16. The microcomputed tomography (Micro-CT) of the specimens in vivo

Bruker Micro-CT Skyscan 1276 system (Kontich, Belgium) was used to scan all specimens. Scan settings were as follows: voxel size 10 μm, medium resolution, 85 kV, 200 mA, 1 mm Al filter and integration time 384 ms. 3D and 2D analysis were performed using software CT Analyser (version 1.18.8.0). Analyses of the bone micro architecture were carried out in a region of interest (ROI).

2.17. Histological staining

At the desired time points, the specimens were obtained and treated for histological analysis. The specimens were fixed with 10% buffered neutralized formalin for 24 h, and then decalcified with 10% EDTA at pH 7.4 for 1 month at room temperature. Then, the specimens were embedded in paraffin after dehydration with gradient alcohol solutions. After being sectioned, the sections were stained with Masson's trichrome, hematoxylin eosin (HE), immunofluorescence targeting CD31 (Abcam, ab64543), α-smooth muscle actin (α-SMA, Abcam, ab240678), ALP (Abcam, ab 224335) and OPN (Abcam, ab8448) to estimate the tissue ingrowth, vascularization and new bone formation at defect sites. The quantitative analyses of those stainning images were performed via Image J.
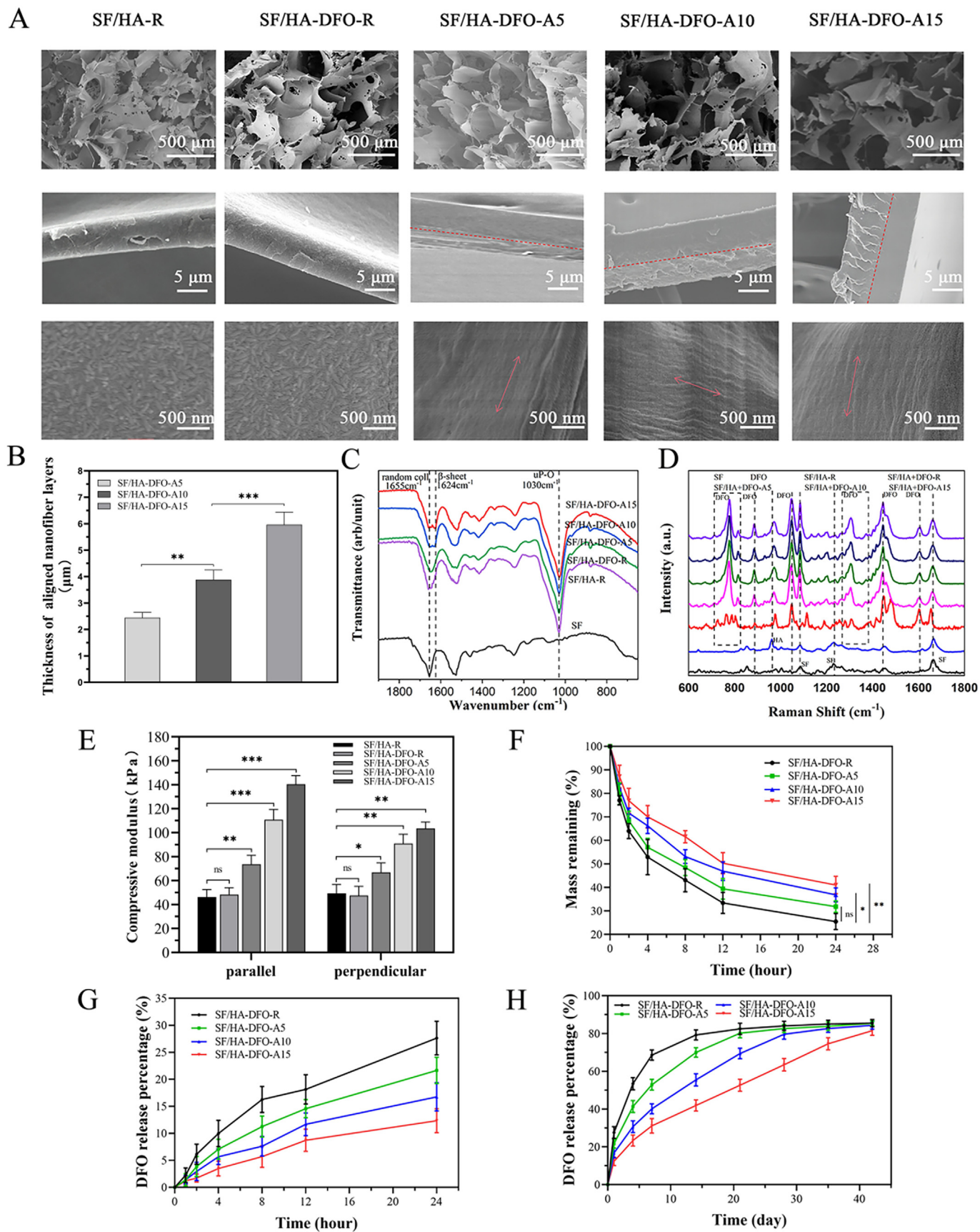
(caption on next page)

Fig. 1. Characterization of the composite scaffolds with tunable SFN layers: (A) SEM images of the different scaffolds. Red dotted lines mean the boundary of aligned SFN layers and porous wall. Red arrows represented the direction of aligned SFN. (B) The thickness of aligned SFN layers when treated for 5, 10, and 15 min under electric field, respectively. (C) FTIR spectra of different scaffolds. (D) Raman spectra of different scaffolds. (E) Compressive modulus of different scaffolds. (F) The degradation behavior of different scaffolds in protease XIV solution. (G, H) DFO release behaviors from the scaffolds. The samples listed as: SF/HA-R, scaffolds composed of HA nanoparticles and silk fibroin; SF/HA-DFO-R, composite SF/HA scaffolds containing DFO; SF/HA-DFO-A5, SF/HA-DFO-R scaffolds with aligned SFN layer treated in electric field for 5 min; SF/HA-DFO-A10, SF/HA-DFO-R scaffolds with aligned SFN layer treated in electric field for 10 min; and SF/HA-DFO-A15, SF/HA-DFO-R scaffolds with aligned SFN layer treated in electric field for 15 min. Data presented as mean ± SD, n = 3, the error bars indicate the SD, p-values are calculated using one-way ANOVA with Sidak's multiple comparison tests, *p < 0.05, **p < 0.01, and ***p < 0.001. NS means no statistical difference (P > 0.05).

2.18. Statistical analysis

All quantitative values were presented as mean ± standard deviation. All results were evaluated by one-way or two-way analysis of variance (ANOVA) followed by Sidak's multiple comparison test (*P < 0.05, **P < 0.01, and ***P < 0.001). *P < 0.05 was considered statistical difference.

3. Results and discussion

3.1. Fabrication of DFO-laden SF-HA composite scaffolds with tunable SFN layers

DFO-laden SF-HA composite scaffolds were endowed with vascularization capacity through the sustained release of DFO. Considering the interaction of DFO and SFNs [38], we anticipated that SFN layers with different thickness would influence DFO release rates from the scaffolds. In our previous study, SFN in aqueous solution migrated directionally and formed laminar hydrogels on positive electrodes under electric field [28,30,39]. The hydrogels grew gradually over time, suggesting the possibility of developing SFN layers with various thicknesses [40]. To evaluate this feasibility, three SF films were placed in different positions inside SFN solution parallel to the electrodes. After treatment under the electric field for 3, 5 and 10 min, the SF films were measured with SEM to reveal the structure and thickness of the formed SFN layers. Layers with similar structure and thickness formed on the films, suggesting homogeneous layers could be prepared inside the SFN solution system (Figure S1 A,B). Following the increase of treatment time, thicker layers appeared on the films (Figure S1 A,B). The results indicated that tunable SFN layers could be generated on the surface of pore walls in the composite scaffolds with the electric field system.

The DFO-laden SF-HA composite scaffolds were immersed in the SFN solution (0.5 wt%) and treated under an electric field for 5, 10 and 15 min, respectively. All the treated scaffolds were kept in the SFN solution for 30 min to avoid different release issues of the DFO from the scaffolds during the treatment process. The amount of DFO released from the different treated scaffolds was similar and below 1% for all three time frames (Figure S2), indicating the vast majority of DFO remained in the scaffolds. Next, the scaffolds were freeze-dried to form the final matrices. According to the treatment time (5, 10 and 15 min), the scaffolds were termed as SF/HA-DFO-A5, SF/HA-DFO-A10, and SF/HA-DFO-A15. Composite scaffolds without electrical field treatment were termed SF/HA-DFO-R (control), while the SF/HA scaffold without DFO was named SF/HA-R (second control). After the treatment, the composite scaffolds maintained their microporous structures without the significant decrease of pore sizes (Fig. 1 A). The pore size of all the scaffolds were above 300 μm, facilitating the cell infiltration. High magnification of the pore walls revealed that the layers with aligned morphology formed inside the pores and adhered on the pore walls (Fig. 1 A). The SFN layers adhered on the pore walls had a thickness from 2.5 μm to 6 μm when the treatment time was increased from 5 to 15 min (Fig. 1A and B). Compared to that formed on silk films (Figure S1), significantly thinner SFN layers formed inside the scaffolds because only the nanofibers inside the pores were migrated to the pore walls. Since the DFO-laden composite scaffolds were composed of amorphous silk while the SFNs had rich beta-sheet content, the electric field treated scaffolds exhibited a significant increase of beta-sheet structure content with increased treatment time, confirming that more SFNs were introduced to the scaffolds

(Fig. 1C) [39]. Similar to previous studies [38,41], the HA nanoparticles (for osteogenic outcomes) dispersed homogeneously in the scaffolds (Fig. 1 A). Raman spectra revealed similar DFO peaks after the electric field treatment, confirming that most of DFO remained within the treated scaffolds (Fig. 1 D). Aligned structures can also result in anisotropic mechanical properties [29]. Beside the increase of compressive modulus from 45 kPa to 140 kPa (Fig. 1 E), significant anisotropic mechanical properties were achieved when higher amounts of aligned SFN layers formed on the treated scaffolds, thus providing mechanical cues for bone regeneration [29]. The introduction of beta-sheet rich SFN layers also improved the stability of the scaffolds. Degradation rate of the scaffolds with thicker SFN layer decreased gradually, which was also beneficial to bone repair (Fig. 1 F, Figure S3) [35]. The typical SEM images of the degraded scaffolds revealed gradual degradation of both SFN layers and porous composite scaffolds (Figure S4). The SFN layers became thinner gradually, which would influence the release behaviors of DFO. Previous study indicated that the SFN had strong physical binding capacity with DFO to reduce the release rate of DFO in aqueous solution [38]. The physical binding of SFN and DFO as well as the physical barrier of the SFN layers were both beneficial to the sustained release of DFO (Fig. 1G and H). As expected, gradually slower release was achieved when more aligned SFN layers were formed on the scaffolds. When the scaffolds were immersed in PBS solution, almost all of the DFO released after 42 days. The release of DFO decreased from 80% to 69%, 55% and 42% after 14 days and also from 84% to 82%, 79% and 63% after 28 days for SF/HA-DFO-R, SF/HA-DFO-A5, SF/HA-DFO-A10 and SF/HA-DFO-A15 samples, respectively. Previous studies suggested that the vascularization capacity of DFO-laden silk matrices was dose dependent [5,31]. Therefore, the regulation of DFO release behavior here implied the possibility of tuning angiogeneisis. Compared to the recent reported studies [21,38], slower release behavior of DFO was achieved in our present study, which could provide the anticipated long-term angiogenic stimulation in bone regeneration process. The sustained release behaviors of DFO were effectively controlled through tuning the thickness of the SFN layers to tune the angiogenesis dynamically, superior to previous bone scaffold systems with vascularization capacity [42,43].

3.2. In vitro cytocompatibility of the composite scaffolds

SF-HA composite scaffolds were biocompatible and have been used to induce bone regeneration [27]. DFO was loaded in SF-HA composite materials to improve vascularization, but at a cost of cytocompatibility [44,45]. Previous studies revealed that free DFO with concentration of above 60 μM in culture medium showed significant cell cytotoxicity [38]. SFN could interact with DFO and restrained the burst release of DFO in water [5,38]. The DFO loaded on SFNs released slowly for above 40 days to induce long-term angiogenesis in wound healing [38]. Based on our recent study [5,38], DFO with concentration of 120 μM in silk nanofiber hydrogels showed better angiogenic capacity without significant cell cytotoxicity. Thus, the DFO concentration maintained 120 μM in the composite scaffold systems to reveal the influence of the sustained release behavior of DFO on the cytocompatibility. According to our reported studies [5,28–30], both cytoskeleton staining and DNA assay were used to evaluate the proliferation behaviors of human umbilical vein endothelial cells (HUVECs) inside the composite scaffolds. Although HUVECs proliferated in all the composite scaffolds, the cells grew more slowly in the DFO-laden scaffolds than that in DFO-free scaffolds (Fig. 2A
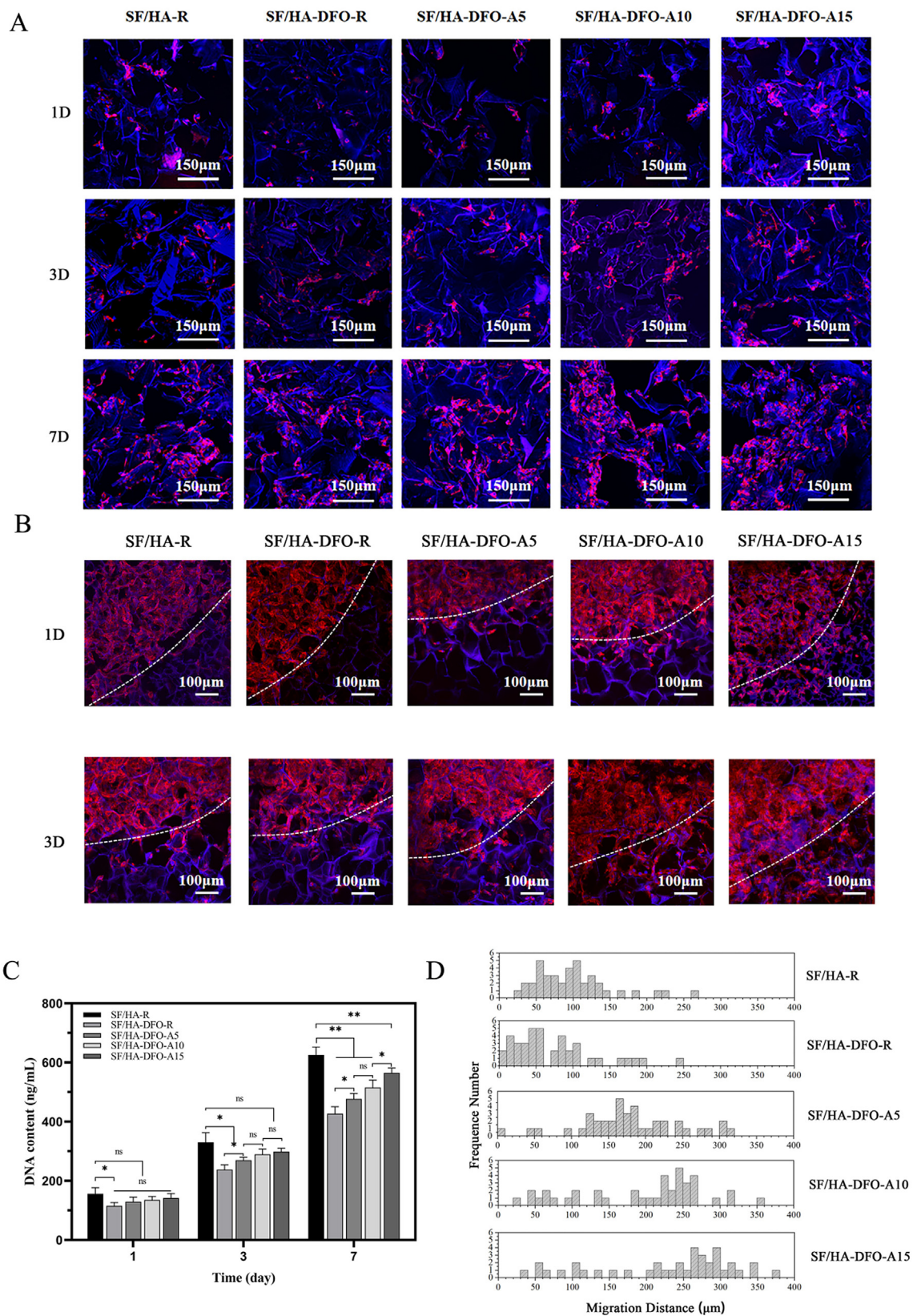
Fig. 2. In vitro cytocompatibility of the composite scaffolds: (A) Confocal microscopy images of HUVECs cultured on the different scaffolds for 1, 3, and 7 days. (B) Migration of endothelial cells on the scaffolds at 1 and 3 days. (C) Proliferation of HUVECs on the scaffolds on day 1, 3 and 7. (D) Frequency distribution of migration distance 0–380 μm after 3 days of culture. Data presented as mean $\pm$ SD, n = 3, the error bars indicate the SD, p-values calculated using one-way ANOVA with Sidak's multiple comparison tests, *$p < 0.05$, **$p < 0.01$, and ***$p < 0.001$. NS means no statistical difference ($P > 0.05$).

and B). The SFN layers slowed the release of DFO and there was significantly improved cell proliferation in the DFO-laden scaffolds with the slower DFO release rate. Besides better cytocompatibility, the aligned SFN layers induced the directional migration of HUVECs, which would also facilitate the cell infiltration and tissue ingrowth [28,36]. At day 3, significant migration was found for the cells cultured on the scaffolds with the aligned layers, while little migration occurred for cells cultured on the SF/HA-R and SF/HA-DFO-R scaffolds (Fig. 2C and D). The best migration occurred for the SF/HA-DFO-A15 group, with longer migration length than in the other DFO-laden scaffolds. Better cytocompatibility and migration behavior should facilitate angiogenesis and bone regeneration, suggesting positive roles for the SFN layers.

3.3. In vitro angiogenesis of HUVECs

DFO stabilized hypoxia inducible factor-1 alpha (HIF-1α) to motivate angiogenesis in bone regeneration [46,47]. To elucidate the influence of slower DFO release on vascularization of the scaffolds, HUVEC tube formation was investigated *in vitro* initially to evaluate the function of the released DFO at 24 h (Fig. 3A and B,C). The highest release rate within 24 h occurred in the DFO-laden scaffolds while the scaffolds coated with the thickest SFN layers showed the slowest release behavior. The assembly of HUVECs exhibited concentration-dependence, where the highest amount of vascular-like structures appeared in the DFO-laden

scaffold group without the SFN layers. The HUVECs were then cultured in the different scaffolds for 35 days and the expression of HIF-1α and vascular endothelial growth factor (VEGF) were measured (Fig. 3D and E). Due to the various DFO release behaviors, dynamic expression of HIF-1α and VEGF occurred. Peak expression of HIF-1α was found for cells cultured in the SF/HA-DFO-R and SF/HA-DFO-A5 scaffolds at day 7, while the cells in the SF/HA-DFO-A10 and SF/HA-DFO-A15 scaffolds had the highest level of expression of HIF-1α at days 21 and 35, respectively. The expression of VEGF was also dynamic, where HUVECs showed the highest expression level at days 7, 21 and 35 when cultured in the SF/HA-DFO-R, SF/HA-DFO-A10 and SF/HA-DFO-A15 scaffolds, respectively. The *in vitro* angiogenesis results confirmed that the aligned SFN layers were an effective regulator to control dynamic rates of vascularization *in vitro* based on morphology and growth rate of features.

3.4. In vitro osteogenic differentiation of BMSCs in composite scaffolds

HA nanoparticles were introduced to the silk scaffolds and hydrogels to improve osteogenic capacity [27,41,48]. Based on our previous studies, the ratio of HA in all the scaffolds was maintained at 40 wt% before silk nanofiber layer formation to provide the optimal osteogenic cues [5,27]. Multiple groups revealed that the loaded DFO stimulated osteodifferentiation of bone mesenchymal stem cells (BMSCs) with improved expression of osteogenic genes (Fig. 4 A-H). In comparison
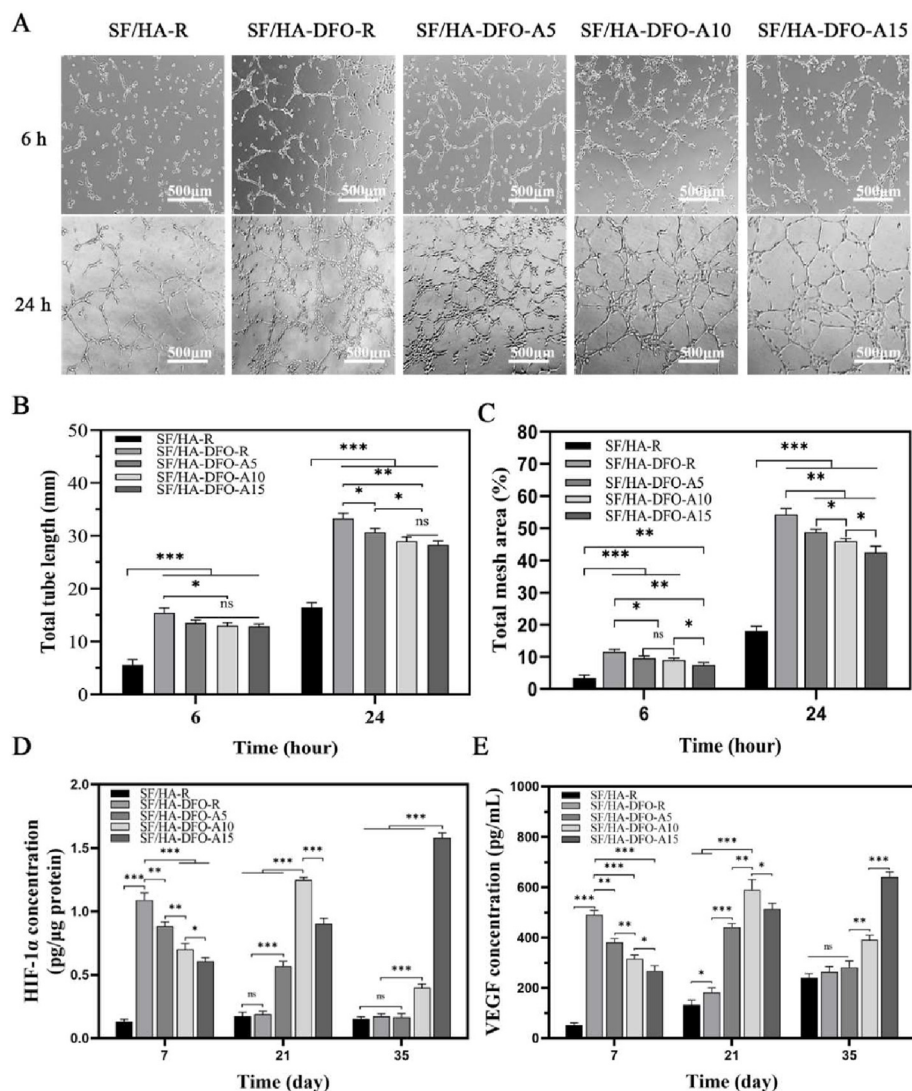
Fig. 3. In vitro vascularization capacity of the composite scaffolds: (A) Images of the endothelial network formation of HUVECs when the cells were cultured with scaffolds for 6 and 24 h. (B) Tube length quantification from different regions. (C) Total mesh area calculated from different scaffold groups. (D) HIF-1α and (E) VEGF expression from HUVECs when the cells were cultured for 7, 21, and 35 days. The data were evaluated with ELISA. Data presented as mean ± SD, n = 3, error bars indicate SD, p-values calculated using one-way ANOVA with Sidak's multiple comparison tests, *p < 0.05, **p < 0.01, and ***p < 0.001. NS means no statistical difference (P > 0.05).
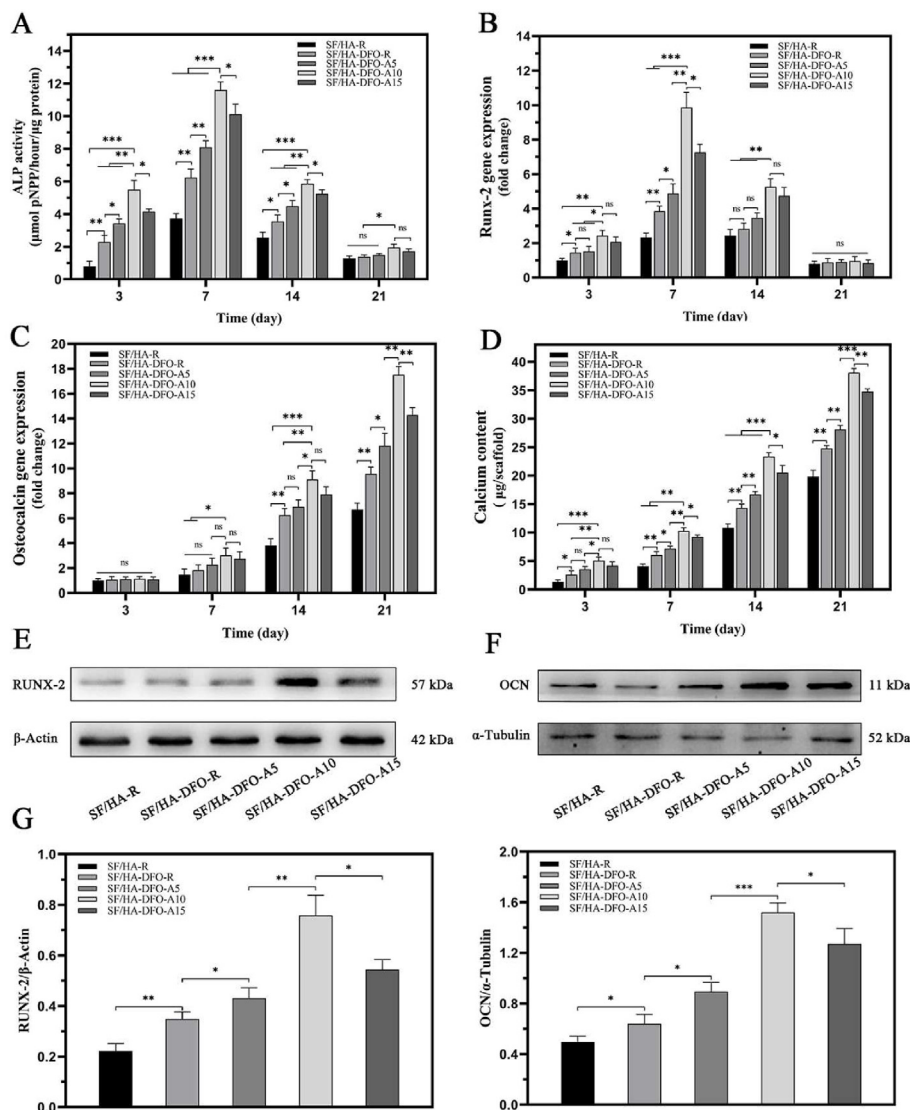
Fig. 4. In vitro osteogenic differentiation of BMSCs on the different scaffolds: (A) alkaline phosphatase activity, (B) mRNA levels of RUNX-2-related transcription factor, (C) osteocalcin, and (D) calcium quantification of BMSCs on day 3, 7, 14, and 21. (E) Western blot results of RUNX-2 on day 7, and (F) Western blot results of OCN on day 21. (G) and (H) The expression of RUNX-2 and OCN calculated from the Western blots. Data presented as mean ± SD, n = 3, error bars indicate the SD, p-values calculated using one-way ANOVA with Sidak's multiple comparison tests, *p < 0.05, **p < 0.01, and ***p < 0.001. NS means no statistical difference (P > 0.05).

with DFO-free SF-HA composite scaffolds, BMSCs exhibited significantly higher expression of alkaline phosphatase (ALP), Runx-2 and osteocalcin (OCN) and higher content of calcium in the cells, confirming the stimulation capacity of DFO in terms of osteodifferentiation (Fig. 4 A-D). The controllable sustained release of DFO further optimized osteogenic capacity, with increased osteogenic gene expression for BMSCs following decreased DFO release rate in the DFO-laden scaffolds, peaked in SF/HA-DFO-A10 scaffolds and decreased in the SF/HA-DFO-A15 scaffolds with the slowest DFO release. Western blots confirmed that the most significant osteodifferentiation was achieved for the BMSCs in the SF/HA-DFO-A10 scaffolds (Fig. 4 E-H). The results indicated that an optimal DFO release behavior stimulated the osteodifferentiation.

3.5. In vivo bone regeneration

A rat femur defect model was filled with different composite scaffolds to assess the influence of different angiogenic and osteogenic features of the scaffolds on bone repair *in vivo*. No death or infection occurred in the rats after scaffold implantation for 12 weeks. Micro-CT images showed different healing rates (Fig. 5 A-E). The control group remained a significant void after 12 weeks, indicating inferior healing capacity. Significantly faster tissue regrowth in the peripheral area of the defect was achieved when the different SF-HA composite scaffolds were implanted. The introduction of DFO and the control of DFO release behavior further improved regeneration of bone tissue. In comparison with SF/HA-R composite scaffolds, the bone volume/total volume ratio (BV/TV) increased from 52% to 78% after 12 weeks (Fig. 5 B). Similar trends occurred for bone mineral density (BMD) and trabecular thickness (Tb.Th) (Fig. 5C,E) in the different groups where the best values were achieved for the defects treated with SF/HA-DFO-A10 scaffolds. The trabecular separation values (Tb. Sp) further confirmed the densest new bone tissues in the defects filled with the SF/HA-DFO-A10 scaffolds. Better osteoid tissue healing occurred through the tuning of DFO release with SFN layers. As expected, the defects treated with SF/HA-DFO-A10 scaffolds with best osteogenic capacity *in vitro* had the highest healing rate *in vivo*, with above 98% of the defects closed after 12 weeks postimplantation, superior to that of the other scaffolds.

The new bone tissues were collected and stained with hematoxylin eosin (HE) after 2, 4, 8 and 12 weeks to confirm regeneration (Fig. 6 A-D, G). The best tissue ingrowth was achieved in the SF/HA-DFO-A10 group (**Figure S**5), which was consistent with the micro-CT results. All of the DFO-laden scaffolds showed better vascularization than the DFO-free scaffolds, and the dynamic regulation of DFO release resulted in different levels of vascularization for the scaffolds containing the same amount of DFO. The best early vascularization at 2 and 4 weeks was achieved for the SF/HA-DFO-A10 scaffolds that stimulated the highest
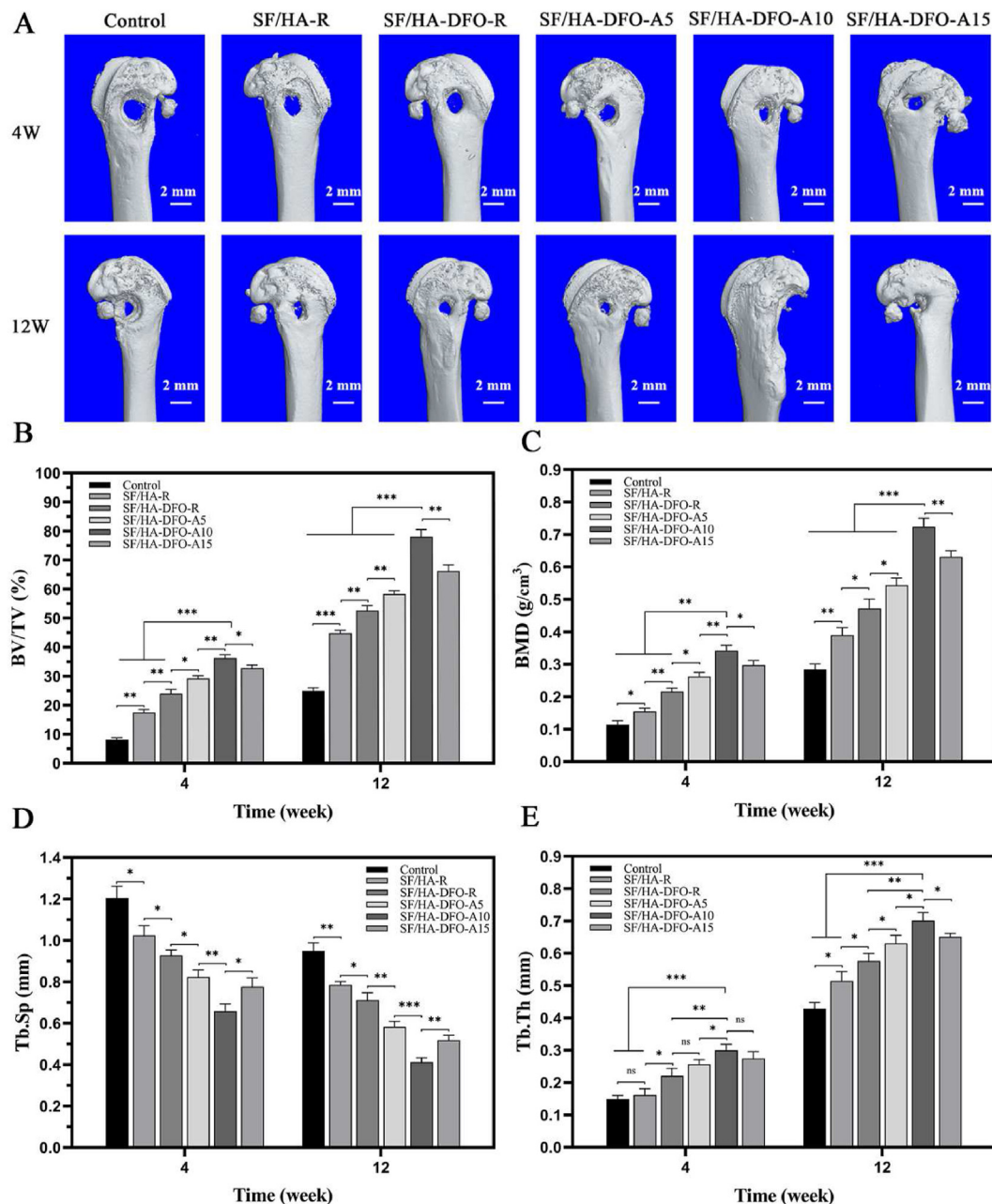
Fig. 5. Micro-CT images and micro-architectural analysis of new bone at defect sites treated with different composite scaffolds: (A) 3D reconstructed images of defect sites at 4 and 12 weeks after implantation. (B) Bone volume/total volume ratio (BV/TV). (C) Bone mineral density (BMD). (D) Trabecular separation (Tb. Sp). (E) Trabecular thickness (Tb. Th). Control defects filled with PBS solution. The other groups were filled with the different composite scaffolds. Data presented as mean ± SD, n = 3, error bars indicate SD, p-values calculated using one-way ANOVA with Sidak's multiple comparison tests, *p < 0.05, **p < 0.01, and ***p < 0.001. NS means no statistical difference (P > 0.05).

VEGF and HIF expression of HUVECs at 3 weeks *in vitro*. After 8 weeks, the highest level of vascularization was found in the defects treated with the SF/HA-DFO-A15 scaffolds that induced the highest VEGF and HIF expression of HUVECs at 5 weeks *in vitro*. The results indicated improved angiogenesis with the SFN layers as regulators of DFO release kinetics, which then resulted in different levels of bone regeneration. At 4 weeks, significant vacant areas maintained at the defects treated with the control group, while new tissues occupied all the defects for the SF/HA-DFO-A10 samples. HE staining also showed different compositions of new tissue in the samples. After 12 weeks post-implantation, more mature bone tissues were regenerated in the defects treated with the SF/HA-DFO-A10 scaffolds, confirming superior bone regeneration.

To further evaluate the angiogenesis in the scaffolds, the collected sections from different samples after 4 and 8 weeks post-implantation were stained with CD31 and α-smooth muscle actin (α-SMA) to visualize angiogenesis (Fig. 6 E-F,H). Although the fluorescence signal of CD31 were weak in all the samples, the α-SMA stained with green showed clear tubular structure of blood vessels to clarify the angiogenesis changes in bone regeneration process. Higher numbers of vessels appeared in the defects treated with the DFO-laden scaffolds, confirming the stimulation by DFO. Similar to the HE results, the highest angiogenesis density in the defects emerged in the SF/HA-DFO-A10 samples after 4 weeks and then in the SF/HA-DFO-A15 samples after 8 weeks. Several studies have suggested that long-term vascularization facilitated
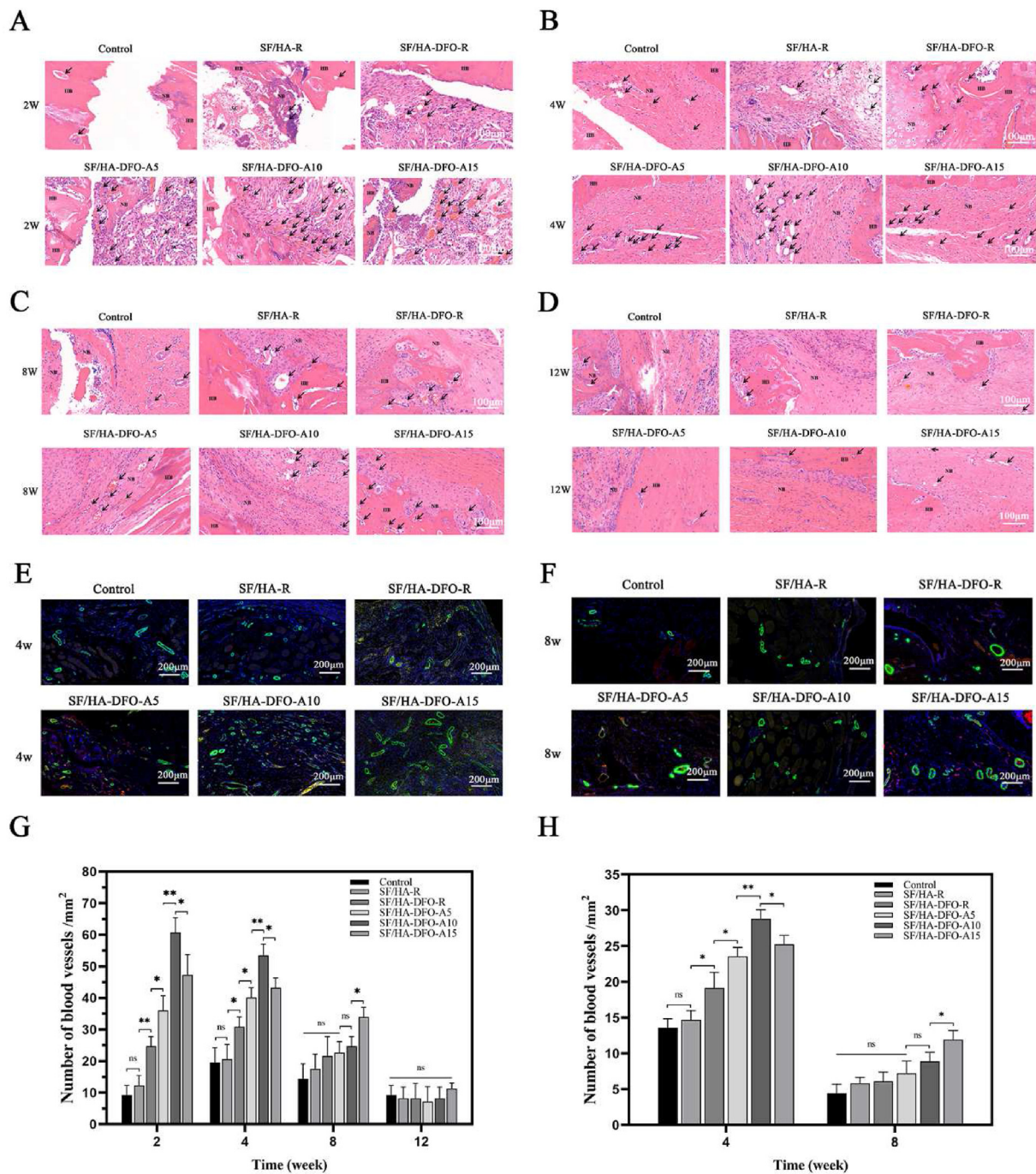
Fig. 6. Neovascularization in the defects: (A–D) H&E staining images of defects treated with different composite scaffolds at weeks 2, 4, 8 and 12 after surgery. Black arrows point to blood vessels, SC indicates implant material, HB means host bone and NB shows newly formed bone. (E, F) The expression of the critical factors relative to the process of angiogenesis at the defects after scaffold implantation for 4 and 8 weeks. CD31 was stained red while α-smooth muscle actin positive cells were stained green. (G) Quantification of vessel number calculated from the images (A–D). (H) Quantification of vessel number calculated from the images (E–F). The control represented the defects filled with PBS solution. The other groups were filled with different composite scaffolds. Data presented as mean ± SD, n = 3, error bars indicate the SD, p-values calculated using one-way ANOVA with Sidak's multiple comparison tests, $*p < 0.05$, $**p < 0.01$, and $***p < 0.001$. NS means no statistical difference ($P > 0.05$).

bone regeneration [49–51]. Through tuning the sustained release of DFO with the SFN layers, control of angiogenesis was achieved, providing effective bone tissue engineering.

The immunofluorescence staining of ALP was used to reveal osteogenic behavior inside the scaffolds at early stages (week 2) (Fig. 7 A,E) [52]. All the DFO-laden scaffold groups exhibited higher ALP expression than the DFO free group and the control group, confirming that the DFO enhanced osteogenic outcomes. Interestingly, significantly higher

expression of ALP was achieved by tuning the DFO release. Although the scaffolds contained the same amount of HA and DFO, the best ALP expression (SF/HA-DFO-A10 sample) was about three times higher than that in the DFO-laden scaffolds without the SFN layers, indicating the critical role of optimal DFO release in the process and outcomes. Based on the *in vitro* and *in vivo* results, we anticipated that suitable DFO release behavior inside the scaffolds provided a desirable niche to co-orchestrate angiogenesis and osteogenesis, surpassing the single stimulation cues
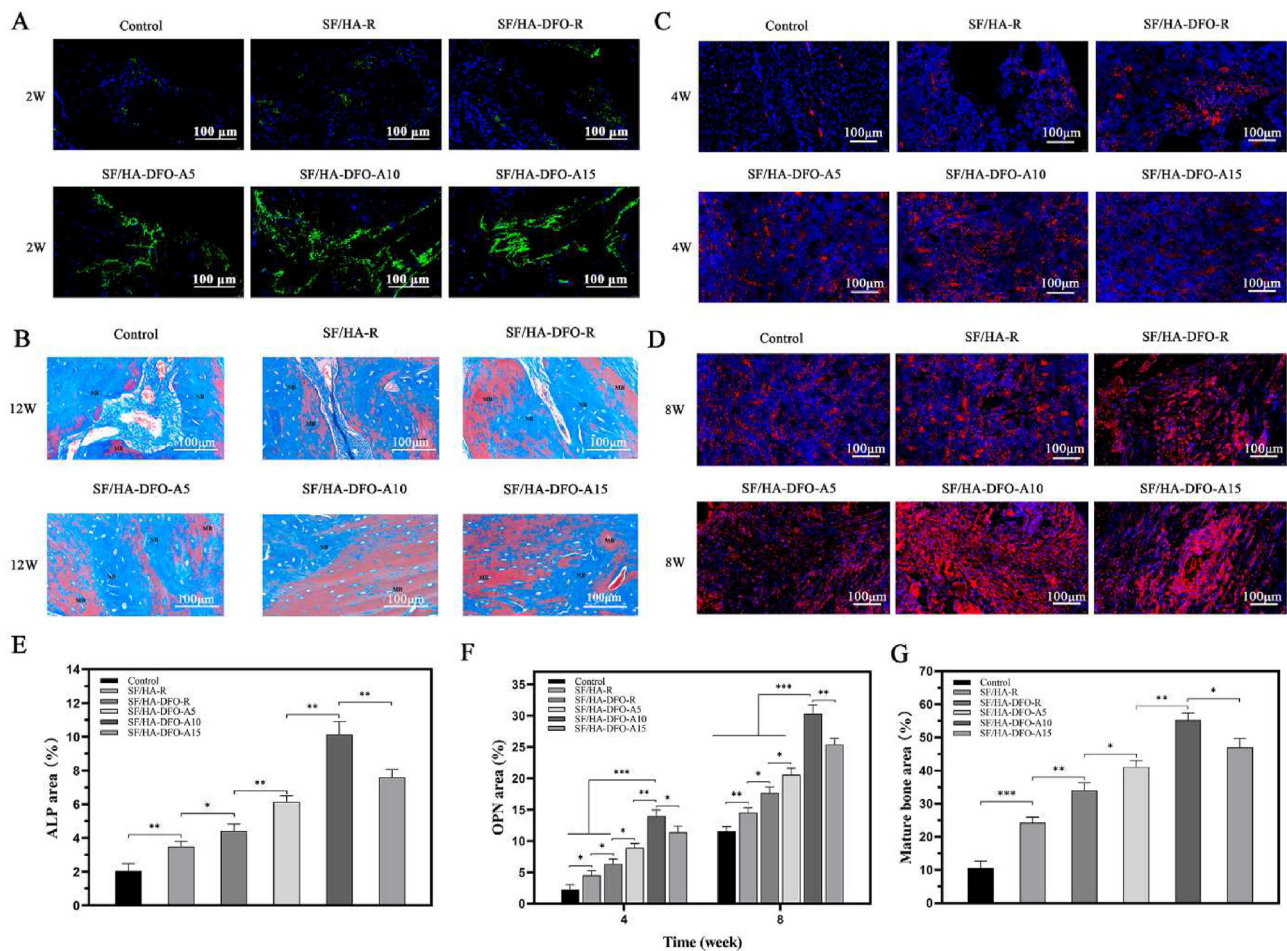
Fig. 7. Quality of regenerated bone in the defects: (A) ALP expression from the tissues grown inside the different composite scaffolds at 2 weeks after surgery. (B) Masson's trichrome staining of the defects treated with different composite scaffolds at 12 weeks after surgery. NB shows new bone formation and MB shows mature bone. (C–D) OPN expression in the defects treated with different composite scaffolds at 4 and 8 weeks after surgery. (E) Quantification of ALP activity calculated from images (A). (F) Quantification of the expression of OPN calculated from images (C–D). (G) Quantification of the mature bone calculated from images (B). Control defects filled with PBS solution. The other groups were filled with the different composite scaffolds. Data presented as mean ± SD, n = 3, error bars indicate SD, p-values calculated using one-way ANOVA with Sidak's multiple comparison tests, *p < 0.05, **p < 0.01, and ***p < 0.001. NS means no statistical difference (P > 0.05).

from DFO and HA. The regenerated bones at the defects were evaluated based on immunofluorescence staining of OPN (Fig. 7 C-D,F), typical marker of mature bones. After 4 and 8 weeks, the highest OPN expression also appeared in the SF/HA-DFO-A10 group that had the best osteogenenic capacity *in vitro*. The quality of the new bone tissue after 12 weeks was also studied through masson's trichrome staining (Fig. 7 B,G). The vacant areas decreased gradually in the control, SF/HA-R, SF/HA-DFO-R, and SF/HA-DFO-A5 groups, and were occupied completely by new bone tissue in the SF/HA-DFO-A10 and SF/HA-DFO-A15 groups. Besides faster filling of the defects, richer collagen deposition and a higher ratio of mature bone was achieved in the SF/HA-DFO-A10 group, confirming the best regeneration quality for this composition.

4. Conclusions

Silk nanofiber layers were utilized to regulate the release behavior of DFO from silk-HA composite scaffolds. The thickness of the layers was regulated by changing the treatment time in the electrical field to control the coating layers, which in turn modulated the release behavior of DFO. Both angiogenenic and osteogenic properties of the scaffolds were optimized in the composite scaffold systems, achieving bone repair. Faster

and better bone regeneration occurred in the composite scaffolds with angiogenesis and osteogenesis features maximized for both outcomes. The results suggest that bioactive bone matrices with optimized vascularization inducement can provide a niche for improved bone regeneration.

Supporting Information

Supporting Information is available from the website or from the author.

Credit author statement

Zhihai Fan, Conceptualization, Investigation, Visualization, Funding acquisition; Hongxiang Liu, Investigation, Writing – original draft; Shilei Shi, Investigation, Validation; Zhaozhao Ding, Conceptualization, Methodology, Formal analysis, Supervision; Zhen Zhang, Resources, Funding acquisition, Resources; Qiang Lu, Conceptualization, Resources, Writing – original draft, Supervision, Project administration; David Kaplan, Writing – review & editing, Supervision, Project administration.

Data availability

The data of this study are available from the corresponding authors on reasonable request.

Declaration of competing interest

The authors declare that they have no known competing financial interests or personal relationships that could have appeared to influence the work reported in this paper.

Acknowledgements

Appendix A. Supplementary data

Supplementary data to this article can be found online at https://doi.org/10.1016/j.mtbio.2022.100283.

References

[1] J. Freitas, S.G. Santos, R.M. Goncalves, J.H. Teixeira, M.A. Barbosa, M.I. Almeida, Genetically engineered-MSC therapies for non-unions, delayed unions and critical-size bone defects, Int. J. Mol. Sci. 20 (2019) 3430.

[2] C.C. Huang, M. Kang, Y. Lu, S. Shirazi, J.I. Diaz, L.F. Cooper, P. Gajendrareddy, S. Ravindran, Functionally engineered extracellular vesicles improve bone regeneration, Acta Biomater. 109 (2022) 182–194.

[3] P. Yang, The role of mesenchymal stem cells in bone regeneration: underlying mechanisms and systemic regulatory factors, Curr. Stem Cell Res. Ther. 12 (2017) 356.

[4] I. Moreno-Jimenez, G. Hulsart-Billstrom, S.A. Lanham, A.A. Janeczek, N. Kontouli, J.M. Kanczler, N.D. Evans, R.O. Oreffo, The chorioallantoic membrane (CAM) assay for the study of human bone regeneration: a refinement animal model for tissue engineering, Sci. Rep. 6 (2016) 32168.

[5] W. Cheng, Z. Ding, X. Zheng, Q. Lu, X. Kong, X. Zhou, G. Lu, D.L. Kaplan, Injectable hydrogel systems with multiple biophysical and biochemical cues for bone regeneration, Biomater. Sci. 8 (2020) 2537–2548.

[6] A.P. Kusumbe, S.K. Ramasamy, R.H. Adams, Coupling of angiogenesis and osteogenesis by a specific vessel subtype in bone, Nature 507 (2014) 323–328.

[7] Q. Yao, Y. Liu, B. Selvaratnam, R.T. Koodali, H. Sun, Mesoporous silicate nanoparticles/3D nanofibrous scaffold-mediated dual-drug delivery for bone tissue engineering, J. Contr. Release 279 (2018) 69–78.

[8] Z. Zhao, X. Ma, J. Ma, J. Kang, Y. Zhang, Y. Guo, Sustained release of naringin from silk-fibroin-nanohydroxyapatite scaffold for the enhancement of bone regeneration, Mater. Today Bio 13 (2022) 100206.

[9] X. Yu, G. Shen, Q. Shang, Z. Zhang, W. Zhao, P. Zhang, D. Liang, H. Ren, X. Jiang, A naringin-loaded gelatin-microsphere/nano-hydroxyapatite/silk fibroin composite scaffold promoted healing of critical-size vertebral defects in ovariectomised rat, Int. J. Biol. Macromol. 15 (2021) 510–518.

[10] I.F. Cengiz, H. Pereira, J. Espregueira-Mendes, I.K. Kwon, R.L. Reis, J.M. Oliveira, Suturable regenerated silk fibroin scaffold reinforced with 3D-printed polycaprolactone mesh: biomechanical performance and subcutaneous implantation, J. Mater. Sci. Mater. Med. 30 (2019) 63–76.

[11] D. Bicho, R.F. Canadas, C. Gonçalves, S. Pina, R.L. Reis, J.M. Oliveira, Porous aligned ZnSr-doped β-TCP/silk fibroin scaffolds using ice-templating method for bone tissue engineering applications, J. Biomater. Sci. Polym. Ed. 32 (2021) 1966–1982.

[12] Z.J. Chen, H.H. Shi, L. Zheng, H. Zhang, Y.Y. Cha, H.X. Ruan, Y. Zhang, X.C. Zhang, A new cancellous bone material of silk fibroin/cellulose dual network composite aerogel reinforced by nano-hydroxyapatite filler, Int. J. Biol. Macromol. 182 (2021) 286–297.

[13] D.W. Li, J. He, F.L. He, Y.L. Liu, Y.Y. Liu, Y.J. Ye, X. Deng, D.C. Yin, Silk fibroin/chitosan thin film promotes osteogenic and adipogenic differentiation of rat bone marrow-derived mesenchymal stem cells, J. Biomater. Appl. 32 (2018) 1164–1173.

[14] Z.N. Mao, X.W. Bi, F. Ye, X. Shu, L. Sun, J. Guan, R.O. Ritchie, S.J. Wu, Controlled cryogelation and catalytic cross-linking yields highly elastic and robust silk fibroin scaffolds, ACS Biomater. Sci. Eng. 6 (2020) 4512–4522.

[15] P. Pripatnanont, C. Chankum, J. Meesane, J. Thonglam, Physical and biological performances of a semi-resorbable barrier membrane based on silk fibroin-glycerol-fish collagen material for guided bone regeneration, J. Biomater. Appl. 36 (2021) 930–942.

[16] P. He, S. Sahoo, K. Chen, S.L. Toh, J.C. Goh, Enhanced osteoinductivity and osteoconductivity through hydroxyapatite coating of silk-based tissue-engineered ligament scaffold, J. Biomed. Mater. Res. 101 (2013) 555–566.

[17] Z.H. Zhao, X.L. Ma, B. Zhao, P. Tian, J.X. Ma, J.Y. Kang, Y. Zhang, Y. Guo, L. Sun, Naringin-inlaid silk fibroin/hydroxyapatite scaffold enhances human umbilical cord-derived mesenchymal stem cell-based bone regeneration, Cell Prolif 54 (2021), e13043.

[18] H. Hong, O.J. Lee, Y.J. Lee, J.S. Lee, O. Ajiteru, H. Lee, Y.J. Suh, M.T. Sultan, S.H. Kim, C.H. Park, Cytocompatibility of modified silk fibroin with glycidyl methacrylate for tissue engineering and biomedical applications, Biomolecules 11 (2020) 35–51.

[19] L.S. Zhu, D. Luo, Y. Liu, Effect of the nano/microscale structure of biomaterial scaffolds on bone regeneration, Int. J. Oral Sci. 12 (2020) 6.

[20] X.M. Ding, M.F. Zhu, B.S. Xu, J.M. Zhang, Y.H. Zhao, S.L. Ji, L.N. Wang, L.Y. Wang, X.L. Li, D.L. Kong, X.L. Ma, Q. Yang, Integrated trilayered silk fibroin scaffold for osteochondral differentiation of adipose-derived stem cells, ACS Appl. Mater. Interfaces 6 (2014) 16696–16705.

[21] X. Zheng, X. Zhang, Y. Wang, Y. Liu, Y. Pan, Y. Li, M. Ji, X. Zhao, S. Huang, Q. Yao, Hypoxia-mimicking 3D bioglass-nanoclay scaffolds promote endogenous bone regeneration, Bioact. Mater. 6 (2021) 3485–3495.

[22] P. Bhattacharjee, B. Kundu, D. Naskar, H.W. Kim, T.K. Maiti, D. Bhattacharya, S.C. Kundu, Silk scaffolds in bone tissue engineering: an overview, Acta Biomater. 63 (2017) 1–17.

[23] X. Li, F. Xiong, S. Wang, Z. Zhang, J. Dai, H. Chen, J. Wang, Q. Wang, H. Yuan, N-Acetyl-Cysteine-Loaded biomimetic nanofibrous scaffold for osteogenesis of induced-pluripotent-stem-cell-derived mesenchymal stem cells and bone regeneration, Front. Bioeng. Biotechnol. 9 (2021) 767641.

[24] D. Burger, M. Beaumont, T. Rosenau, Y. Tamada, Porous silk fibroin/cellulose hydrogels for bone tissue engineering via a novel combined process based on sequential regeneration and porogen leaching, Molecules 25 (2020) 5097.

[25] K. Kucharczyk, A. Florczak, T. Deptuch, K. Penderecka, K. Jastrzebska, A. Mackiewicz, H. Dams-Kozlowska, Drug affinity and targeted delivery: double functionalization of silk spheres for controlled doxorubicin delivery into Her2-positive cancer cells, J. Nanobiotechnol. 18 (2020) 56–63.

[26] L. Zeng, L. Jiang, W. Teng, J. Cappello, Y. Zohar, X. Wu, Engineering aqueous fiber assembly into silk-elastin-like protein polymers, Macromol. Rapid Commun. 35 (2014) 1273–1279.

[27] B. He, J. Zhao, Y. Ou, D. Jiang, Biofunctionalized peptide nanofiber-based composite scaffolds for bone regeneration, Mater Sci Eng C Mater Biol Appl 90 (2018) 728–738.

[28] G. Lu, Z. Ding, Y. Wei, X. Lu, Q. Lu, D.L. Kaplan, Anisotropic biomimetic silk scaffolds for improved cell migration and healing of skin wounds, ACS Appl. Mater. Interfaces 10 (2018) 44314–44323.

[29] G. Xu, Z. Ding, Q. Lu, X. Zhang, X. Zhou, L. Xiao, G. Lu, D.L. Kaplan, Electric field-driven building blocks for introducing multiple gradients to hydrogels, protein cell, Protein Cell 11 (2020) 267–285.

[30] Q. Lu, F. Zhang, W. Cheng, X. Ga, Z. Ding, X. Zhang, Q. Lu, D.L. Kaplan, Nerve guidance conduits with hierarchical anisotropic architecture for peripheral nerve regeneration, Adv. Healthcare Mater. 10 (2021), e2100427.

[31] C. Wan, S.R. Gilbert, Y. Wang, X. Cao, X. Shen, G. Ramaswamy, K.A. Jacobsen, Z.S. Alaql, A.W. Eberhardt, L.C. Gerstenfeld, T.A. Einhorn, L. Deng, T.L. Clemens, Activation of the hypoxia-inducible factor-1 alpha pathway accelerates bone regeneration, Proc. Natl. Acad. Sci. U.S.A. 105 (2008) 686–691.

[32] X.W. Huang, S.M. Bai, Q. Lu, X. Liu, S.S. Liu, H.S. Zhu, Osteoinductive-nanoscaled silk/HA composite scaffolds for bone tissue engineering application, J. Biomed. Mater. Res. B 103 (2015) 1402–1414.

[33] S.S. Lin, G.Z. Lu, S.S. Liu, S.M. Bai, X. Liu, Q. Lu, B.Q. Zuo, D.L. Kaplan, H.S. Zhu, Nanoscale control of silks for nanofibrous scaffold formation with an improved porous structure, J. Mater. Chem. B 2 (2014) 2622–2633.

[34] Z.S. Zhang, Z.Z. Ding, J.W. Huang, J.Z. Qin, Y.X. Shen, F. Zhang, B.Q. Zuo, Green process to prepare water-insoluble silk scaffolds with silk I structure, Int. J. Biol. Macromol. 117 (2018) 144–151.

[35] F. Han, S. Liu, X. Liu, Y. Pei, S. Bai, H. Zhao, Q. Lu, F. Ma, D.L. Kaplan, H. Zhu, Woven silk fabric-reinforced silk nanofibrous scaffolds for regenerating load-bearing soft tissues, Acta Biomater. 10 (2014) 921–930.

[36] X. Lu, Z. Ding, F. Xu, Q. Lu, D.L. Kaplan, Subtle regulation of scaffold stiffness for the optimized control of cell behavior, ACS Appl. Bio Mater. 2 (2019) 3108–3119.

[37] H. Chen, P. Jia, H. Kang, H. Zhang, Y. Liu, P. Yang, Y. Yan, G. Zuo, L. Guo, M. Jiang, J. Qi, Y. Liu, W. Cui, H.A. Santos, L. Deng, Upregulating hif-1α by hydrogel nanofibrous scaffolds for rapidly recruiting angiogenesis relative cells in diabetic wound, Adv. Healthcare Mater. 5 (2016) 907–918.

[38] Z. Ding, M. Zhou, Z. Zhou, W. Zhang, X. Jiang, X. Lu, B. Zuo, Q. Lu, D.L. Kaplan, Injectable silk nanofiber hydrogels for sustained release of small-molecule drugs and vascularization, ACS Biomater. Sci. Eng. 5 (2019) 4077–4088.

[39] Z. Ding, G. Lu, W. Cheng, G. Xu, B. Zuo, Q. Lu, D.L. Kaplan, Tough anisotropic silk nanofiber hydrogels with osteoinductive capacity, ACS Biomater. Sci. Eng. 6 (2020) 2357–2367.

[40] Q. Lu, S. Bai, Z. Ding, H. Guo, Z. Shao, H. Zhu, D.L. Kaplan, Hydrogel assembly with hierarchical alignment by balancing electrostatic forces, Adv. Mater. Interfac. 3 (2016) 1500687.

[41] Z.Z. Ding, Z.H. Fan, X.W. Huang, S.M. Bai, D.W. Song, Q. Lu, D.L. Kaplan, Bioactive natural protein-hydroxyapatite nanocarriers for optimizing osteogenic differentiation of mesenchymal stem cells, J. Mater. Chem. B 4 (2016) 3555–3561.

[42] H.F. Pereira, I.F. Cengiz, F.S. Silva, R.L. Reis, J.M. Oliveira, Scaffolds and coatings for bone regeneration, J. Mater. Sci. Mater. Med. 31 (2020) 27–32.

[43] X. Han, M. Sun, B. Chen, Q. Saiding, J. Zhang, H. Song, L. Deng, P. Wang, W. Gong, W. Cui, Lotus seedpod-inspired internal vascularized 3D printed scaffold for bone tissue repair, Bioact. Mater. 6 (2020) 1639–1652.

[44] Z.J. Liu, R. Tian, Y. Li, L. Zhang, H. Shao, C. Yang, O.C. Velazquez, SDF-1α-Induced dual pairs of E-selectin/ligand mediate endothelial progenitor cell homing to critical ischemia, Sci. Rep. 6 (2016) 34416.

[45] V.L. Nguyen, C.T. Truong, B.C.Q. Nguyen, T.V. Vo, T.T. Dao, V.D. Nguyen, D.T. Trinh, H.K. Huynh, C.B. Bui, Anti-inflammatory and wound healing activities of calophyllolide isolated from Calophyllum inophyllum linn, PLoS One 12 (2017), e0185674.

[46] K.K. Chereddy, R. Coco, P.B. Memvanga, B. Ucakar, A. des Rieux, G. Vandermeulen, V. Preat, Combined effect of PLGA and curcumin on wound healing activity, J. Contr. Release 171 (2013) 208–215.

[47] Q. Yao, Y. Liu, J. Tao, K.M. Baumgarten, H. Sun, Hypoxia-mimicking nanofibrous scaffolds promote endogenous bone regeneration, ACS Appl. Mater. Interfaces 8 (2016) 32450–32459.

[48] P. Holden, L.S. Nair, Deferoxamine: an angiogenic and antioxidant molecule for tissue regeneration, Tissue Eng. B Rev. 25 (2019) 461–470.

[49] F.A. Auger, L. Gibot, D. Lacroix, The pivotal role of vascularization in tissue engineering, Annu. Rev. Biomed. Eng. 15 (2013) 177–200.

[50] Y. Yan, H. Chen, H. Zhang, C. Guo, K. Yang, K. Chen, R. Cheng, N. Qian, N. Sandler, Y.S. Zhang, H. Shen, J. Qi, W. Cui, L. Deng, Vascularized 3D printed scaffolds for promoting bone regeneration, Biomaterials **190–191** (2019) 97–110.

[51] L. Krishnan, N.J. Willett, R.E. Guldberg, Vascularization strategies for bone regeneration, Ann. Biomed. Eng. 42 (2014) 432–444.

[52] S. Watari, K. Hayashi, J.A. Wood, P. Russell, P.F. Nealey, C.J. Murphy, D.C. Genetos, Modulation of osteogenic differentiation in hMSCs cells by submicron topographically-patterned ridges and grooves, Biomaterials 33 (2012) 128–136.